Dynamical magnetostructural properties of *Anabaena* ferredoxin

Eduard Schreiner*[†], Nisanth N. Nair*, Rodolphe Pollet*[‡], Volker Staemmler*, and Dominik Marx*

*Lehrstuhl für Theoretische Chemie, Ruhr-Universität Bochum, 44780 Bochum, Germany; and [‡]Laboratoire Francis Perrin, Commissariat à l'Energie Atomique, 91191 Gif-sur-Yvette, France

A mixed quantum/classical investigation of the dynamical magnetostructural properties, that is, "magnetodynamics," of oxidized *Anabaena* PCC7119 ferredoxin is carried out at room temperature in two distinct conformational states. This protein hosts a [2Fe–2S] cluster in which two iron centers are antiferromagnetically coupled to an overall low-spin electronic ground state that has a genuine multireference character. To study the magnetodynamics of this prosthetic group, an approximate spin projection method is formulated in the framework of density functional theory that allows for multideterminant *ab initio* molecular dynamics simulations to be carried out efficiently. By using this scheme, the influence of both thermal fluctuations and conformational motion on the structure of the [2Fe–2S] cluster and on the dynamics of the antiferromagnetic coupling constant, $J(t)$, has been investigated. In addition to demonstrating how sensitively the shape of the [2Fe–2S] core itself is affected by hydrogen bonding, the analyses reveal a complex dynamical coupling of J to both local vibrations and large-amplitude motion. It is shown that this interplay can be understood in terms of specific vibrational modes and distinct hydrogen-bonding patterns between the iron–sulfur cluster and the protein backbone, respectively. This implies going beyond the Goodenough–Kanamori rules for angular magnetostructural correlations of oxidized iron–sulfur prosthetic groups.

exchange coupling | extended broken-symmetry | hydrogen bonding | iron–sulfur protein | multideterminant hybrid molecular dynamics

Iron–sulfur clusters are among the most ubiquitous, functionally versatile, and ancient prosthetic groups in proteins (1–4). One of the major classes of mobile electron carriers in contemporary biology is ferredoxin (Fd). Its fourfold cysteine-coordinated [2Fe–2S] core mediates electron transfer from photosystem I to ferredoxin-NADP$^+$-oxidoreductase, which reduces NADP$^+$ to NADPH. A particularly interesting system is Fd from cyanobacterium *Anabaena* PCC7119 whose crystal structure was recently obtained at 1.3 and 1.17 Å resolution in the oxidized and the reduced forms (5), respectively. Most interestingly, it was found that two alternative conformations of Cys-46 exist, which is one of the four cysteinyl ligands of the [2Fe–2S] cluster (5). In the oxidized state Cys-46 adopts the so-called CO-in conformation, where the peptide oxygen points in the direction of the cluster, whereas, on reduction, the backbone flips to the CO-out conformation.

Spin Coupling in Iron–Sulfur Clusters. In the ground state of the oxidized form of bioinorganic [mFe–nS] clusters, the Fe^{3+} metal centers are typically in a local high-spin d^5 configuration [i.e., S_{Fe} = 5/2 for ferric Fe(III) centers], whereas they themselves are antiferromagnetically coupled to yield an overall low-spin state due to dominant superexchange interactions (6). In particular, the electronic ground state of [2Fe–2S] clusters in Fd has genuine multireference character and makes computational studies challenging (6). The electronic structure is described most conveniently by the broken-symmetry (BS) state. At the heart of this approach is a one-determinant spin-polarized (unrestricted) representation where the two sets of electrons localized on the two transition metal centers are kept in an antiparallel spin arrangement. Clearly, this state features enormous spin contamination and, because it is not an eigenstate of the total (coupled) spin operator, it does not represent the true low-spin antiferromagnetic ground state (7). Alternatively, sophisticated quantum-chemical methods can be used to describe the coupled state, which suffer, however, from having to take into account both "static" (multireference-induced) and "dynamic" (interelectron cusp-induced) electron correlation (8–10). Computationally this implies severe limitations in terms of system size and coupling to molecular dynamics (MD). A well established compromise in terms of cost versus accuracy are spin-projection schemes (11, 12) that rely on an approximate purification of the spin state (13) by carrying out independent total energy calculations for several uncoupled spin configurations (14, 15). Such approaches allow the calculation of the exchange coupling constant J directly and have been proven to perform particularly well for binuclear homovalent clusters in static calculations (16, 17).

Iron–Sulfur Clusters in Proteins. When it comes to [2Fe–2S] embedded in a protein such as Fd, quantum-chemical calculations have been performed to estimate redox potentials (18, 19) or reorganization energies (20). Recently, there were attempts to understand the conformational changes (5) of *Anabaena* PCC7119 Fd by using density functional theory (DFT) calculations (21). All of these calculations were performed by using static structures. However, it has been shown most recently for rubredoxin (Rd) that a molecular description of the environment is crucial (22); note that Rd features only a single-Fe center and thus no magnetic interactions. For large systems like proteins, mixed quantum/classical MD offers a particularly suited and efficient way to take such effects into account (23, 24).

Magnetodynamics of Iron–Sulfur Proteins. Thus, when aiming at understanding iron–sulfur proteins it is inevitable to consider temperature effects, protein conformational motions, solvent interactions, and, most importantly, it is mandatory to properly describe the antiferromagnetic electronic ground state. Here, we introduce a general computational technique by which the antiferromagnetic ground-state structure and the dynamics of (binuclear homovalent) transition metal clusters in proteins at realistic conditions can be obtained efficiently in the framework of mixed quantum/classical MD in combination with an extended spin-projection formalism. By using this procedure, dynamical magnetostructural properties, that is, "magnetodynamics," of the oxidized [2Fe–2S] cluster in fully solvated *Anabaena* PCC7119 Fd have been investigated in its CO-in and CO-out conformations at room

BIOPHYSICS

CHEMISTRY

temperature. Detailed insights into the relationships of magnetic properties and structural dynamics, including the conformational influence of the protein environment, are thus obtained. In particular, it is possible to go beyond the Goodenough–Kanamori rules (6), which fail to predict angular magnetostructural properties of such d^5–d^5 binuclear clusters.

The Extended Broken Symmetry Formalism. Phenomenologically, the exchange coupling in homovalent magnetic dimers can be modeled by the Heisenberg Hamiltonian (6)

$$\hat{H} = -2J\hat{S}_A\hat{S}_B = -J(\hat{S}^2 - \hat{S}_A^2 - \hat{S}_B^2) \qquad [1]$$

where $\hat{S}_A$ and $\hat{S}_B$ are effective local spin operators for the coupled sites A and B with associated quantum numbers S_A and S_B, respectively, $\hat{S} = \hat{S}_A + \hat{S}_B$ is the total (coupled) spin operator, and J is the exchange (magnetic) coupling constant. This Hamiltonian generates a spin-ladder of eigenstates with total (coupled) spin quantum number S ranging from $S_{max} = S_A + S_B$ (high-spin, HS) down to $S_{min} = |S_A - S_B|$ (low-spin, LS). The total energy E^S of a spin-coupled state with total spin quantum number S is

$$E^S = -J[S(S + 1) - S_A(S_A + 1) - S_B(S_B + 1)].$$

For given S_A and S_B this gives rise to Landé's interval rule, $E^S - E^{S-1} = -2JS$, which allows one to calculate the energies of *all* spin states if J and the total energy of one state is known. To calculate these quantities one needs the exact Clebsch–Gordan-coupled eigenstates $|S_A S_B; S\ M\rangle$ of the used many electron Hamiltonian. If, however, the coupled eigenstates are not exactly known, as often encountered in computational approaches, it is very useful to evaluate the expectation value of the total spin operator

$$E^S = -J[\langle\hat{S}^2\rangle^S - S_A(S_A + 1) - S_B(S_B + 1)], \qquad [2]$$

using approximately coupled states.

A way to estimate the coupling constant J by using Landé's rule in conjunction with E^{HS} and E^{BS} was put forward a long time ago (11, 12, 25), which is concisely reformulated and extended here. The HS and BS states are single-determinant states characterized by parallel and antiparallel alignment of spins on the two coupled paramagnetic sites, respectively. Their total energies, E^{HS} and E^{BS}, are easily accessible by using a single Slater or Kohn–Sham spin-polarized (unrestricted) determinant and are written as:

$$E^{HS/BS} = -J[\langle\hat{S}^2\rangle^{HS/BS} - S_A(S_A + 1) - S_B(S_B + 1)] \qquad [3]$$

in the spirit of Eq. **2**. By using Eq. **3** together with Landé's rule it can be shown readily that, because of

$$J = \frac{E^{BS} - E^{HS}}{\langle\hat{S}^2\rangle^{HS} - \langle\hat{S}^2\rangle^{BS}}, \qquad [4]$$

J can be obtained from theses energies (25). Based on Löwdin's exact expression (26) for the total spin of an N-electron system (of N^α and N^β spin up and down electrons) using the two-particle density matrix Γ and its formulation (27) in terms of off-diagonal elements one obtains

$$\langle\hat{S}^2\rangle = \left(\frac{N_{mag}^\alpha - N_{mag}^\beta}{2}\right)\left(\frac{N_{mag}^\alpha - N_{mag}^\beta}{2} + 1\right) + N_{mag}^\beta + \Theta \qquad [5]$$

with

$$\Theta = N_{nmag}^\beta + 2\int \Gamma(\mathbf{r}_1\alpha,\ \mathbf{r}_2\beta|\mathbf{r}_1\beta,\ \mathbf{r}_2\alpha)d\mathbf{r}_1 d\mathbf{r}_2.$$

Here, $N^\alpha + N^\beta = N$ with $N^\alpha \geq N^\beta$, $N_{nmag}^\sigma + N_{mag}^\sigma = N^\sigma$, $N_{nmag/mag}^\sigma$ is the number of paired/unpaired (i.e., "nonmagnetic/magnetic") σ-electrons, and

$$\Gamma(\mathbf{x}_1',\ \mathbf{x}_2'|\mathbf{x}_1,\ \mathbf{x}_2) = \frac{N(N - 1)}{2}$$

$$\times \int \psi^*(\mathbf{x}_1',\ \mathbf{x}_2',\ \ldots,\mathbf{x}_N')\psi(\mathbf{x}_1,\ \mathbf{x}_2,\ \ldots,\mathbf{x}_N)$$

$$d\mathbf{x}_3\ \ldots\ d\mathbf{x}_N d\mathbf{x}_3'\ \ldots\ d\mathbf{x}_N',$$

where $\mathbf{x}_i = (\mathbf{r}_i, \sigma_i)$ is the combined spatial and spin coordinate of electron i; Eq. **5** has been given in terms of N^α and N^β in ref. 27. The physical meaning of the *exact* expression Eq. **5**, which does not rely on any orbital picture, is best revealed in the *approximation* to Θ in the framework of unrestricted Hartree–Fock theory (28)

$$\Theta = N_{nmag}^\beta - \sum_i^N \sum_j^N f_i^\alpha f_j^\beta\langle\phi_i^\alpha|\phi_j^\beta\rangle^2 \qquad [6]$$

and noting that $\Theta = 0$ and thus $\langle\hat{S}^2\rangle = S(S + 1)$ when the *exact* solution of Eq. **1**, that is, the pure spin state of the coupled system, is used; $f_i^\sigma = \{0, 1\}$ is the occupation number of spin orbital ϕ_i^σ. Thus, Θ is a "correction term" that takes into account the overlap of magnetic (unpaired) orbitals and spin contamination when $\langle\hat{S}^2\rangle^{HS/BS}$ is evaluated in expressions like Eq. **4**. In addition, this view opens up a simple and unified pathway to derive systematically further approximations to turn the scheme into a computationally practical approach, *vide infra*. Importantly, Θ can also be formulated approximately within DFT (27) and thus it can be used as an alternative in the formulae for J and c given below.

Putting all this together a general expression for J can thus be written as

$$J = \frac{E^{BS} - E^{HS}}{(S_{max} - S_{min})(S_{max} + S_{min}) - \Theta^{BS} + \Theta^{HS}} \qquad [7]$$

in terms of the two determinants. For an equal number of α- and β-electrons, and assuming strong localization (i.e., no overlap of magnetic orbitals), Θ is zero so that Eq. **7** reduces to the well known formula introduced by Noodleman (12). However, other formulae used in the literature (29, 30) can easily be derived as special cases of strong/weak localization and the total number of unpaired electrons. Last but not least, finite overlap could also be taken into account approximately in the spirit of a systematic improvement.

Crucial for our purpose is the observation that, based on Eq. **2**, the total energy of the low-spin ground state itself, E^{LS}, can be reformulated with the help of Eq. **7** in terms of the HS and BS total energies as

$$E^{LS} = (1 + c)E^{BS} - cE^{HS} = \mathcal{P}E^{BS,HS}, \qquad [8]$$

where $\mathcal{P}$ projects the energy of the low-spin state from the energies of the two single-determinant BS and HS states and c is given by

$$c = \frac{S_{max} - S_{min} + \Theta^{BS}}{(S_{max} - S_{min})(S_{max} + S_{min}) - \Theta^{BS} + \Theta^{HS}} \qquad [9]$$

for homovalent binuclear clusters. Next, having obtained such a closed expression for the total LS energy, forces, and thus an *ab initio* MD (31) approach

$$M_I\ddot{\mathbf{R}}_I = -\nabla_I\mathcal{P}E^{BS,HS} \qquad [10]$$

can be introduced for antiferromagnetically coupled spin dimers in terms of a two-determinant expression of its total energy. The gains

Table 1. Selected averages of structural properties and *J* of the iron–sulfur cluster obtained from MD *in vacuo* and in the solvated protein in the CO-in and CO-out conformations compared with experimental X-ray diffraction data

	$Fe_2S_2(SH)_4^{2-}$*	Fd_{in}[†]	Fd_{out}[†]	Fd_{in}[‡]
Distance, A				
Fe–Fe	2.64	2.62	2.62	2.75
S1–S2	3.46	3.51	3.52	3.52
Fe1–S1	2.18	2.22	2.21	2.28
Fe1–S2	2.17	2.16	2.19	2.23
Fe2–S1	2.17	2.22	2.21	2.23
Fe2–S2	2.18	2.17	2.18	2.18
Angle, °				
S1–Fe1–S2	105.2	106.3	106.2	102.2
S1–Fe2–S2	105.3	105.9	106.5	105.6
Fe1–S1–Fe2	74.8	72.2	72.5	75.1
Fe1–S2–Fe2	74.7	74.3	73.5	76.8
S2–Fe1–S1–Fe2	0.1	8.4	8.7	4.3
J, cm^{-1}	−403	−386	−360	—

For results obtained *in vacuo*, the enumeration of the atoms is arbitrary because of symmetry. See ref. 5.
*In vacuo.
[†]Solvated protein.
[‡]X-ray diffraction data.

of this extended broken-symmetry (EBS) scheme are twofold. It is possible, first of all, to optimize the structure of such antiferromagnetic clusters and, second, to study their dynamics by means of MD, which is our main interest. Finally, we note in passing that these expressions can be generalized to heterovalent and polynuclear magnetic centers.

Next, neglecting spin contamination and assuming strong localization of magnetic orbitals, thus neglecting their mutual overlap, Eq. **9** simplifies to

$$c = \frac{S_{max} - S_{min}}{(S_{max} - S_{min})(S_{max} + S_{min})} \qquad [11]$$

with the corresponding LS total energy Eq. **8**. This special case is identical to that exploited by Noodleman and coworkers (19), but can be improved systematically depending on the approximation to Θ. At this stage, we can formulate *ab initio* MD very efficiently in the framework of a generalized Car–Parrinello Lagrangian (31, 32)

$$\mathcal{L}_{CP}^{LS} = \frac{1}{2}\sum_I M_I \dot{\mathbf{R}}_I^2 + \frac{1}{2}\sum_i \mu \, \mathcal{P}\langle \dot{\psi}_i | \dot{\psi}_i \rangle^{BS,HS} - \mathcal{P}E^{BS,HS}$$

$$+ \sum_{S=BS,HS}\sum_{i,j} \Lambda_{ij}^S (\langle \psi_i^S | \psi_j^S \rangle - \delta_{ij}) \qquad [12]$$

by which classical nuclear dynamics can be performed on the antiferromagnetically coupled low-spin ground state energy hypersurface. Here, M_I is the nuclear mass of the *I*th nucleus and μ is the fictitious electron mass parameter. Note that the BS and HS determinants, and thus the two sets of orbitals $\{\psi_i^{BS}\}$ and $\{\psi_i^{HS}\}$, are simultaneously propagated under the constraint that orthonormality is satisfied individually.

The EBS scheme so far allows the propagation of an isolated [2Fe–2S] cluster, thus calling for a coupling to force fields to take the protein environment into account. The coupling approach used here is based on the CPMD/Gromos QM/MM interface (33). Because the LS charge density is not known, it is crucial to obtain *all* contributions to hierarchical electrostatics (33) consistently with the chosen projection scheme (Eq. **8**).

Results and Discussion

Before addressing the central issue of magnetodynamics, average structures obtained from *ab initio* MD of the iron–sulfur cluster *in vacuo* and as a prosthetic group are compared in Table 1; concerning equilibrium structures *in vacuo*, it is noted in passing that using the approximately spin-projected low-spin total energy, that is, Eq. **8** with Eq. **11**, for structure optimization, instead of the heavily spin-contaminated single-determinant E^{BS} potential energy surface, leads to slightly more compact $Fe_2S_2(SH)_4^{2-}$ and to 10% larger $|J|$ values. The average structure of the [2Fe–2S] moiety is fairly symmetric and planar *in vacuo*, whereas it is best described as a nonplanar and distorted lozenge within the biomolecular environment. The observed asymmetry of the [2Fe–2S] core in the CO-in conformer is in accordance with experimental x-ray data (5) where it has been connected to an asymmetry in the hydrogen bond network. Our simulations also show different bond distances within the [2Fe–2S] cluster that can clearly be traced back to the hydrogen-bonding topology involving the iron–sulfur cluster and peptide hydrogen atoms as seen in Fig. 1*a*. Although it has been suggested that the S2-HN(Cys-46) hydrogen bond exists only in the reduced state of Fd (5), the present simulations clearly show that this is also the case for the oxidized state.

In the CO-out conformation the pattern of hydrogen bonds between the core and the backbone differs significantly (see Fig. 1*b*). Each of the sulfur atoms has three hydrogen bonds, but of considerably different lengths. The asymmetry in the bond distances within the Fe1-S1-Fe2 and the Fe1-S2-Fe2 moieties is also present in the CO-out conformation, although to a lesser extent than in the CO-in case. Overall, these data show how intimately the structure of such iron–sulfur cofactors is coupled to the particular hydrogen bond pattern spanned by the protein.

Furthermore, the data compiled in Table 1 demonstrate that the cluster is less compact in Fd and that the average value of *J* is decreased therein, thus showing a direct influence of the protein
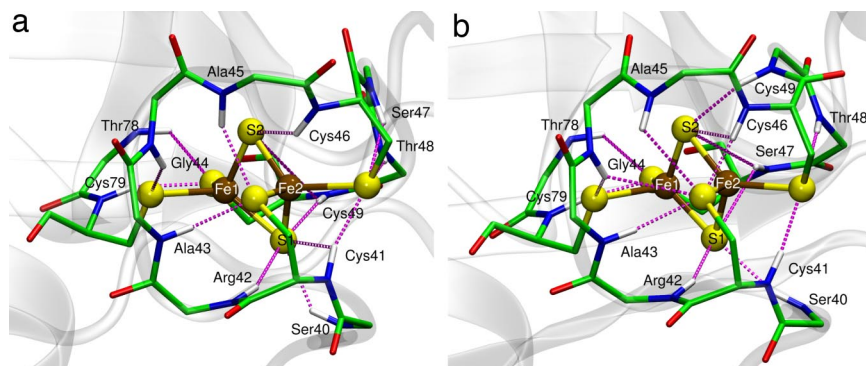
Fig. 1. Local environment of the iron–sulfur cluster in *Anabaena* Fd CO-in (*a*) and CO-out (*b*) conformer. The oxygen atoms are red, nitrogen atoms are blue, carbon atoms are green, and hydrogen atoms are white. The yellow and brown spheres represent sulfur and iron atoms, respectively. Hydrogen bonds are indicated by dotted purple lines.
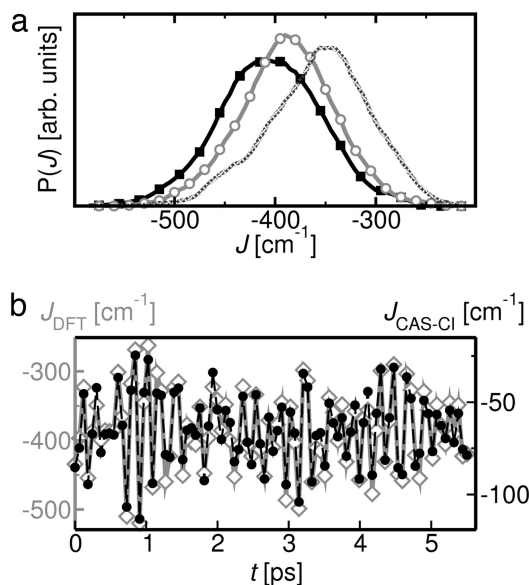
Fig. 2. Behavior of J obtained from EBS-MD and CAS-CI calculations. (*a*) Comparison of the probability distribution of J obtained from EBS simulations for the iron–sulfur cluster *in vacuo* (filled squares) to the distribution in solvated Fd in its CO-in (open circles) and CO-out (patterned line) conformations. (*b*) Comparison of dynamics $J(t)$ as obtained from DFT EBS-QM/MM simulation (open diamonds, solid line, left scale) with those from CAS-CI calculations (filled circles, dashed line, right scale); see text for details.

environment. At the same time, the difference in the average value of J for the CO-in and CO-out conformations reveals the influence of different protein environments. It is also interesting to observe that the amplitude of J fluctuations is larger in the CO-out conformation than in the CO-in (see Fig. 2*a*).

Experimental values of J for *Anabaena* Fd are not available, but similar proteins like spinach Fd yield values between -183 cm^{-1} (34, 35) and -145 cm^{-1} (36). Overestimation of the absolute value of J by about a factor of two is a well known problem in DFT when using generalized gradient approximations (7). It is a direct result of the self-interaction error leading to artificially delocalized magnetic orbitals, which should not be confused with the consequences of proper spin-projection as lucidly discussed in ref. 7. To cure this deficiency on a theoretically sound basis both spin-projection and self-interaction correction must be taken into account (7), that is, by using hybrid functionals (37, 38) or by employing constrained DFT procedures (39). But in view of the additional computational complexity we presently do not follow this route; instead, we compare the dynamical EBS data with very elaborate, complete active-space configuration interaction (CAS-CI) calculations to assess their quality. To this end, approximately 100 structures of the *ab initio* fragment are sampled from the trajectory of the CO-in conformer and, for each of them, J has been computed by both EBS and CAS-CI. First, CAS-CI confirms explicitly the validity of the phenomenological spin Hamiltonian Eq. **1** by computing explicitly its energy levels. Thus, even in the fluctuating Fd environment, the spin eigenstates are found to obey Landé's pattern within 2% (data not shown), thus yielding Heisenberg's spin-ladder rather than imposing it *a priori*. Furthermore, according to Fig. 2*b*, the behavior of $J(t)$ provided by EBS is extremely well reproduced by CAS-CI. However, this high-level wavefunction-based calculation now underestimates J compared with experiment, which is a well understood phenomenon because the orbitals determined in the Hartree–Fock method underlying the CAS-CI calculations underestimate the Fe–S covalency and overestimate the energies of the d^4–d^6 charge transfer states.

After having demonstrated that the EBS approach leads to a good description of the dynamics of the exchange coupling constant, $J(t)$, its connections to structural motions and thus the dynamical magnetostructural properties can be analyzed. It is gratifying that the calculated vibrational power spectrum for the iron–sulfur cluster as well as its spectral decomposition are in agreement with recent resonance Raman data (40). A true magnetodynamical quantity, which is accessible with our technique, is the power spectrum $J(\omega)$ in Fig. 3*a*, as obtained for the iron–sulfur cluster *in vacuo* as well as for the CO-in and CO-out conformers of Fd. Apparently, the sharp single peak present at $\approx 160 \text{ cm}^{-1}$ *in vacuo* becomes broad and blue-shifted in the protein. Additionally, in the CO-in conformation the spectrum between 260 and 450 cm^{-1} is more complex than *in vacuo*, whereas for the CO-out case the J spectrum exhibits one asymmetric peak at $\approx 370 \text{ cm}^{-1}$. Moreover, in both Fd conformers we observe some high-frequency components in $J(\omega)$ at $\approx 3,320 \text{ cm}^{-1}$.

To understand this complex dynamics we relate the features of $J(\omega)$ to specific vibrational modes of the [2Fe–2S] core. Taking into account the approximate D_{2h} symmetry of the [2Fe–2S] average structure *in vacuo*, it is appropriate to use symmetry-adapted orthonormal modes as basis. Apart from overall rotations and translations of all four atoms in space, six internal modes exist, but only a subset is found to drive the magnetodynamics of the prosthetic group of Fd. The coupling is revealed in Fig. 3*b–d* by presenting the frequency-dependent cross-correlations between J and the relevant normal modes in addition to the power spectra. *In vacuo* the two totally symmetric modes that describe the innercore vibrations in terms of angles ($A_{g,A}$) and distances ($A_{g,D}$) are sufficient to explain the dynamics of J. Whereas the former accounts for the low-frequency part, the latter can be associated with the region between 300 and 450 cm^{-1}. The appearance of a double peak for the $A_{g,D}$ breathing mode and thus also in $J(\omega)$ is attributed to a coupling of $A_{g,D}$ to the Fe–SH ligand vibrations.

In the protein, Fd, the situation is much more complicated. In the region between 70 and 260 cm^{-1}, the J spectrum becomes broad and is blue-shifted. Analysis shows that in addition to the $A_{g,A}$ mode ($\approx 190 \text{ cm}^{-1}$) the $B_{1g,oop}$ out-of-plane vibration strongly correlates with J at $\approx 160^{-1}$. At first sight, the appearance of the latter contribution may be due to the asymmetry of the cluster in Fd because of hydrogen bonding. However, this mode shows no strong correlation to J in the CO-out case, although the cluster is also asymmetric there. Thus, the correlation of $B_{1g,oop}$ with J must be due to the coupling of other modes to $B_{1g,oop}$.

Between 260 and 450 cm^{-1}, we observe contributions from B_{2u} and $B_{1g,ip}$ in-plane vibrations apart from those of $A_{g,D}$. Naively, one would not expect J to be affected by these modes (6): motion along the B_{2u} mode enhances one superexchange pathway while destroying the other one, whereas both pathways are destroyed along the $B_{1g,ip}$ mode. This picture indeed holds very well for the cluster *in vacuo*. However, because the structure is asymmetric in Fd, the above argumentation does not apply, at least not for B_{2u}. To resolve this situation we also analyzed the mutual coupling of the different modes. It turns out that the B_{2u} mode is only very weakly coupled to $A_{g,D}$, which is reflected in the small feature in the $A_{g,D}$-J correlation at $\approx 400 \text{ cm}^{-1}$. In contrast to that, the $B_{1g,ip}$ vibration shows strong coupling to both A_g modes which is reflected in their frequency-dependent J cross-correlations. It is interesting that, for the CO-out conformation, the $B_{1g,ip}$ contribution disappears completely and also B_{2u} affects $J(\omega)$ only to a very small extent, indicating a different coupling pattern among the modes.

Finally, there are the intriguing high-frequency components of $J(\omega)$ at $\approx 3,320 \text{ cm}^{-1}$ that must stem from an ultrafast modulation of $J(t)$. Obviously, none of the core vibrations themselves can account for this behavior. As shown in Fig. 1 the iron–sulfur cluster in Fd is connected to the protein matrix by various hydrogen bonds in addition to the strong covalent cysteine links. In particular, hydrogen bonding between the bridging sulfur atoms of the cluster,
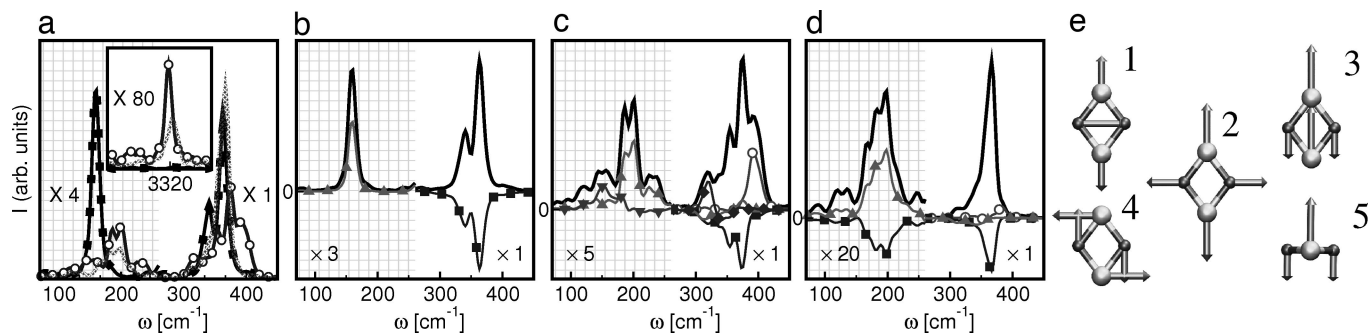
Fig. 3. Magnetostructural dynamics of the oxidized binuclear iron–sulfur cluster. (*a*) Power spectra $J(\omega)$ for the cluster obtained *in vacuo* (filled squares) and within Fd in its CO-in (open circles) and CO-out (patterned solid line) conformation. The gray area indicates the spectral range in which the intensity is enhanced by a factor of 4 for clarity. (*Inset*) The spectra in the range 3,200 to 3,400 cm^{-1}. The intensity of the spectra is scaled by a factor of 80. Power spectra of J together with the frequency-dependent correlations of J and the motion along relevant modes of the [2Fe–2S] subsystem *in vacuo* (*b*) and within Fd in its CO-in (*c*) and CO-out conformation (*d*). The gray regions indicate a scaling of the spectra by the given factor. These relevant normal modes are shown in *e*. The arrows show the phases and relative magnitudes of the atomic displacements, but the actual displacements are enlarged for the sake of clarity. Dark and light spheres represent iron and sulfur atoms, respectively. Symbol code: 1, $A_{g,A}$ (filled triangles); 2, $A_{g,D}$ (filled squares); 3, B_{2u} (open circles); 4, $B_{1g,ip}$ (filled diamonds); 5, $B_{1g,oop}$ (filled inverted triangles).

S1 and S2, and hydrogen atoms of the peptide groups of the backbone influences the electronic structure of the iron–sulfur cluster. Indeed, a correlation analysis suggests a direct relationship between the corresponding S–H distances and the exchange coupling constant J. In particular, we find that in the CO-in conformation of Fd the interactions between Cys-46 and S1 most notably influence J. Additionally, Cys-49 forms a hydrogen bond that oscillates between S1 and S2. None of these hydrogen bonds seems to be related to J in the CO-out structure where instead Ser-40 and Ser-47 NH groups play the decisive role by directly interacting with S1 and S2, respectively.

Having demonstrated that magnetodynamical quantities such as $P(J)$ and $J(\omega)$ provide a wealth of insights into the magnetic interactions, it remains to be discussed how they could be measured. High-resolution inelastic neutron scattering is a powerful technique to directly measure intensity profiles due to exchange splittings in complex molecular clusters (41, 42), which can be directly related to $P(J)$ of Fig. 2*a* for a given splitting if the isotropic Heisenberg model holds. Second, the frequency-dependent modulation of J due to dynamical motion giving rise to rich power spectra $J(\omega)$ in Fig. 3 can be probed in the spirit of action spectroscopy. The change of $P(J)$ (measured by inelastic neutron scattering) that is induced by concurrently exciting vibrational modes with strong electromagnetic radiation is recorded by scanning the excitation frequency ω in the infrared regime. This gives rise to resonances only at those frequencies ω where the modulation is most pronounced, which are the peaks of $J(\omega)$. Alternatively, the ω-dependent excitation could be achieved by nuclear inelastic scattering of synchrotron radiation at Mössbauer-active nuclei which is already established for intramolecular vibrational spectroscopy that is sensitive to exclusively those modes that involve Fe nuclei (43, 44).

Summary and Conclusions. To understand the properties of antiferromagnetically coupled binuclear transition metal clusters, we introduced an efficient two-determinant Car–Parrinello *ab initio* MD scheme based on a spin projection technique that extends the traditional description by using the broken-symmetry approach. Using this method, we investigated the magnetostructural dynamics of an oxidized binuclear iron–sulfur cluster in *Anabaena* PCC7119 Fd in two conformational states, CO-in and CO-out, at room temperature.

The cluster is symmetric *in vacuo*, whereas in the protein matrix the local hydrogen bond network distorts its structure to a higher degree in the CO-in than in the CO-out form. Importantly, the protein environment not only affects the magnitude of the exchange coupling but also modulates its dynamics.

Thermal fluctuations are found to be able to change J by $\approx 50\%$

from its average value. In all cases investigated, the dynamics of the exchange coupling constant $J(t)$ and thus the gross structure of the resulting power spectrum $J(\omega)$ can be understood in terms of $A_{g,A}$ and $A_{g,D}$ symmetry-adapted normal modes due to cluster vibrations. However, there is conformation-specific fine structure: within the CO-in conformation in Fd the B_{2u} symmetric mode also directly affects J and, in addition, the two B_{1g} modes modulate $J(t)$ by coupling to the A_g modes, which is in contrast to the CO-out conformer. Furthermore, there is a high-frequency component at $J(\omega) \approx 3,300$ cm^{-1} in the protein that can be traced back to very specific hydrogen bonds, namely, Cys-46-S1 and Cys-49-S2 in the CO-in conformer and Ser-40-S1 and Ser-47-S2 in the CO-out Fd.

To conclude, the results presented lead to a deep understanding of the dynamic magnetostructural properties of oxidized iron–sulfur prosthetic groups. They confirm the expected dependence of J on the Fe–S distance within the core, but allow one to transcend the well established Goodenough–Kanamori rules (6) for the angular behavior. In particular, the dependence of $J(t)$ on essentially only two symmetry-adapted modes, $A_{g,A}$ and $A_{g,D}$, suggests the possibility to parameterize the exchange coupling constant as a function of these most crucial internal coordinates.

Methods

Force Field and System Setup. The protein model is based on the oxidized *Anabaena* PCC7119 Fd (5) (PDB ID code 1qt9; chain B) assuming standard protonation states and solvation with 13265 TIP3P water molecules while retaining the water molecules from the crystal structure and adding 23 Na$^+$ and 5 Cl$^-$ to establish a neutral system. Protein interactions are described by using AMBER94 (45) and the partial charges of the [2Fe–2S] core were determined by Bader analysis (46) of the BS density of [Fe$_2$S$_2$(SH)$_4$]$^{2-}$ *in vacuo*, yielding 0.9385 and -0.7303 for Fe and S, respectively. To maintain charge neutrality in the QM/MM setup, the partial charges of the C$_\alpha$, H$_\alpha$, and S$_\gamma$ atoms were adapted accordingly. The nonbonding interactions for Fe were obtained from a published heme group (47), whereas cysteinyl parameters were used for S.

Hybrid Simulations. The hybrid QM/MM simulations (23, 24) were carried out by using the CPMD/Gromos interface (33) within the CPMD program package (31, 48; see also www.cpmd.org), both extended by the EBS scheme. The QM fragment consisted of the [2Fe–2S] cluster core supplemented by the S$_\gamma$, C$_\beta$, and H$_\beta$ atoms of the four cysteinyl ligands; the dangling bonds at C$_\beta$ were saturated by using capping H atoms constrained to the C$_\alpha$–C$_\beta$ connecting line. The QM fragment was described within spin-unrestricted Kohn–Sham DFT in its plane wave/pseudopotential formulation (31). The PBE functional (49, 50) was chosen and the core electrons were taken into account by ultrasoft pseudopotentials (51) at a cutoff of 30 Ry containing additional *d*-projectors in case of S as well as scalar relativistic corrections and semicore states for Fe. Finite cluster boundary conditions (52) were imposed on a large cubic simulation box of 40 a.u. with a total charge of $-2e$. Car–Parrinello propagation (32) was performed with a time step

of 4 a.u. ($\approx$0.12 fs) by using a fictitious orbital mass parameter of 500 a.u. and substituting the H masses by D. Separate Nosé–Hoover chain thermostats (53) at 300 K were coupled to the nuclei and atoms in the QM and MM systems, respectively, in addition to thermostating separately the set of HS and BS orbitals. After equilibration of $\approx$3 ps trajectories of $\approx$16 and 12 ps were collected for the CO-in and CO-out conformations, respectively. Reference simulations of $[Fe_2S_2(SH)_4]^{2-}$ where carried out *in vacuo* for approximately 5 + 18 ps by using similar parameters.

Power spectra of vibrations and $J(\omega)$ were computed from Fourier transforms of velocity and J time-autocorrelation functions, respectively, and were quantum-corrected by using the ''harmonic quantum correction factor'' (54). Cross-correlations were obtained after projecting the nuclear coordinates on orthogonal modes normalized to unity variance. These latter modes were calculated by transforming the D_{2h} symmetry-adapted modes such as to minimize the cross-correlation of the corresponding projections of the trajectory.

Configuration Interaction Calculations. Close to 100 configurations of the QM subsystem were sampled (every 60 fs from the EBS-QM/MM trajectory of the CO-in conformer) for which CAS-CI calculations within an active space spanned by the 10 singly occupied Fe d-orbitals were carried out by using orbitals from restricted open-shell Hartree–Fock calculations of the HS determinant. To compensate for the known underestimation of superexchange by CAS-CI, J was obtained by formula 11 in ref. 55. with $\alpha = 2.93$ calculated by using the scheme of refs. 55 and 56. The basis set had approximately triple-zeta quality, was augmented by various diffuse functions (augVTZPP), and consisted of 500 functions.

1. Hall DO, Cammack R, Rao KK (1971) *Nature* 233:136–138.
2. Beinert H, Holm RH, Münck E (1997) *Science* 277:653–659.
3. Rees DC, Howard JB (2003) *Science* 300:929–931.
4. Johnson DC, Dean DR, Smith AD, Johnson MK (2005) *Annu Rev Biochem* 74:247–281.
5. Morales R, Chron MH, Hudry-Clergeon G, Pétillot Y, Norager S, Medina M, Frey M (1999) *Biochemistry* 38:15764–15773.
6. Kahn O (1993) *Molecular Magnetism* (VCH, New York).
7. Adamo C, Barone V, Bencini A, Broer R, Filatov M, Harrison NM, Illas F, Malrieu JP, de Pinho Ribeiro Moreira I (2006) *J Chem Phys* 124:107101-1–107101-3.
8. Fink K, Fink R, Staemmler V (1994) *Inorg Chem* 33:6219–6229.
9. Wang C, Fink K, Staemmler V (1995) *Chem Phys* 201:87–94.
10. Hübner O, Sauer J (2002) *J Chem Phys* 116:617–628.
11. Yamaguchi K, Yoshioka Y, Takatsuka T, Fueno T (1978) *Theor Chim Acta* 48:185–206.
12. Noodleman L (1981) *J Chem Phys* 74:5737–5743.
13. Yamaguchi K, Jensen F, Dorigo A, Houk KN (1988) *Chem Phys Lett* 149:537–542.
14. Noodleman L, Lovell T, Liu T, Himo F, Torres RA (2002) *Curr Opin Chem Biol* 6:259–273.
15. Shoji M, Koizumi K, Taniguchi T, Kitagawa Y, Yamanaka S, Okumura M, Yamaguchi K (2007) *Int J Quant Chem* 107:116–133.
16. Noodleman L, Peng CY, Case DA, Mouesca JM (1995) *Coord Chem Rev* 144:199–244.
17. Hübner O, Sauer J (2002) *Phys Chem Chem Phys* 4:5234–5243.
18. Mouesca JM, Chen JL, Noodleman L, Bashford D, Case DA (1994) *J Am Chem Soc* 116:11898–11914.
19. Li J, Nelson MR, Peng CY, Bashford D, Noodleman L (1998) *J Phys Chem A* 102:6311–6324.
20. Sigfridsson E, Olsson MHM, Ryde U (2001) *Inorg Chem* 40:2509–2519.
21. Morales R, Frey M, Mouesca JM (2002) *J Am Chem Soc* 124:6714–6722.
22. Sulpizi M, Raugei S, VandeVondele J, Carloni P, Sprik M (2007) *J Phys Chem B* 111:3969–3976.
23. Rousseau R, Kleinschmidt V, Schmitt UW, Marx D (2004) *Angew Chem Int Ed* 43:4804–4807.
24. Mathias G, Marx D (2007) *Proc Natl Acad Sci USA* 104:6980–6985.
25. Yamaguchi K, Fukui H, Fueno T (1986) *Chem Lett* 15:625–628.
26. Löwdin PO (1955) *Phys Rev* 97:1474–1489.
27. Wang J, Becke AD, Smith VH Jr (1995) *J Chem Phys* 102:3477–3480.
28. Neese F (2004) *J Phys Chem Solids* 65:781–785.
29. Caballol R, Castell O, Illas F, de Pinho Ribeiro Moreira I, Malrieu JP (1997) *J Phys Chem A* 101:7860–7866.
30. Ruiz E, Cano J, Alvarez S, Alemany P (1999) *J Comp Chem* 20:1391–1400.
31. Marx D, Hutter J (2000) in *Modern Methods and Algorithms of Quantum Chemistry*, ed Grotendorst J (John von Neumann Institute for Computing, Jülich, Germany), Vol 3, pp 301–449.
32. Car R, Parrinello M (1985) *Phys Rev Lett* 55:2471–2474.
33. Laio A, VandeVonde J, Rothlisberger U (2002) *J Chem Phys* 116:6941–6947.
34. Palmer G, Dunham WR, Fee JA, Sands RH, Iizuka T, Yonetani T (1971) *Biochim Biophys Acta* 245:201–207.
35. Dunham WR, Palmer G, Sands RH, Bearden AJ (1971) *Biochim Biophys Acta* 253:373–384.
36. Benini S, Ciurli S, Luchinat C (1995) *Inorg Chem* 34:417–420.
37. Martin RL, Illas F (1997) *Phys Rev Lett* 79:1539–1542.
38. Ruiz E, Alemany P, Alvarez S, Cano J (1997) *J Am Chem Soc* 119:1297–1303.
39. Rudra I, Wu Q, van Voorhis T (2006) *J Chem Phys* 124:024103-1–024103-9.
40. Rotsaert FAJ, Pikus JD, Fox BG, Markley JL, Sanders-Loehr J (2003) *J Biol Inorg Chem* 8:318–326.
41. Jayasooriya UA, Cannon RD, White RP, Stride JA, Grinter R, Kearley GJ (1993) *J Chem Phys* 98:9303–9310.
42. Sieber A, Foguet-Albiol D, Waldmann O, Ochsenbein ST, Bircher R, Christou G, Fernandez-Alonso F, Mutka H, Güdel HU (2005) *Inorg Chem* 44:6771–6776.
43. Paulsen H, Winkler H, Trautwein AX, Grünsteudel H, Rusanov V, Toftlund H (1999) *Phys Rev B* 59:975–984.
44. Paulsen H, Rusanov V, Benda R, Herta C, Schünemann V, Janiak C, Dorn T, Chumakov AI, Winkler H, Trautwein AX (2002) *J Am Chem Soc* 124:3007–3011.
45. Cornell WD, Cieplak P, Bayly CI, Gould IR, Merz KM, Ferguson DM, Spellmeyer DC, Fox T, Caldwell JW, Kollman PA (1995) *J Am Chem Soc* 117:5179–5197.
46. Henkelman G, Arnaldsson A, Jónsson H (2006) *Comput Mater Sci* 36:354–360.
47. Giammona DA (1994) PhD thesis (Univ of California, Davis, CA).
48. IBM, Max Plank Institute (2006) CPMD (IBM, Armonk, NY, and Max Plank Institute, Stuttgart, Germany) version 3.10.
49. Perdew JP, Burke K, Ernzerhof M (1996) *Phys Rev Lett* 77:3865–3868.
50. Perdew JP, Burke K, Ernzerhof M (1997) *Phys Rev Lett* 78:1396–1396.
51. Vanderbilt D (1990) *Phys Rev B* 41:7892–7895.
52. Martyna GJ, Tuckerman ME (1999) *J Chem Phys* 110:2810–2821.
53. Martyna GJ, Klein ML, Tuckerman M (1992) *J Chem Phys* 97:2635–2643.
54. Ramírez R, López-Ciudad T, Kumar P, Marx D (2004) *J Chem Phys* 121:3973–3983.
55. Fink K, Wang C, Staemmler V (1999) *Inorg Chem* 38:3847–3856.
56. Staemmler V, Fink K (2002) *Chem Phys* 278:79–87.

Schreiner *et al.*